Journal of Laser Applications

RESEARCH ARTICLE | SEPTEMBER 23 2024

Laser powder bed fusion of pure copper using ring-shaped beam profiles

Special Collection: Proceedings of the International Congress of Applications of Lasers & Electro-Optics (ICALEO 2024)

Alexander Bauch ; Philipp Kohlwes ; Ingomar Kelbassa

J. Laser Appl. 36, 042021 (2024)
https://doi.org/10.2351/7.0001562

Journal of Laser Applications ARTICLE pubs.aip.org/lia/jla

Laser powder bed fusion of pure copper using ring-shaped beam profiles

Cite as: J. Laser Appl. 36, 042021 (2024); doi: 10.2351/7.0001562
Submitted: 28 June 2024 · Accepted: 29 August 2024 ·
Published Online: 23 September 2024

Alexander Bauch,[1] Philipp Kohlwes,[1] and Ingomar Kelbassa[1,2]

AFFILIATIONS

[1]Fraunhofer Research Institution for Additive Manufacturing Technologies IAPT, Am Schleusengraben 14, Hamburg 21029, Germany
[2]Hamburg University of Technology, Institute for Industrialization of Smart Materials ISM, Eißendorfer Straße 40, Hamburg 21073, Germany

Note: Paper published as part of the special topic on Proceedings of the International Congress of Applications of Lasers & Electro-Optics 2024.

ABSTRACT

Additive manufacturing of copper using laser powder bed fusion (PBF-LB/M) enables the production of highly complex components. However, processing of copper by means of near-infrared laser radiation is challenging due to its absorptivity of only 5%–20%. Using a keyhole welding process with a Gaussian intensity distribution increases the absorptivity up to 53% due to multireflection. This enables the production of components with a density larger than 99.5% and electrical conductivity larger than 90% of the International Annealed Copper Standard (IACS), but this type of welding leads to keyhole porosity due to keyhole instabilities. One way of counteracting is the use of a heat conduction welding process. However, due to the Gaussian intensity distribution, it is not possible to supply sufficient energy to eliminate lack-of-fusion porosity and concurrently avoid the formation of a keyhole. Ring-shaped beam profiles have proven their advantages in stabilizing the PBF-LB/M process with a tendency toward higher laser power, but pure copper has not yet been processed in this way. Therefore, this study investigates the potential of three ring-shaped beam profiles to produce specimens with a density of more than 99.5% and their respective electrical conductivity using a laser power of up to 1300 W. In order to understand the underlying welding process, the weld geometry of single-tracks is analyzed. Specimens with a density of up to 99.77% and an electrical conductivity of up to 101.62% IACS are produced, whereby the material properties and welding regime depend on the selected ring-shaped beam profile.

Key words: beam shaping, laser powder bed fusion, pure copper, near-infrared laser radiation, additive manufacturing

I. INTRODUCTION

Copper is widely used for heat sinks, heat exchangers, and induction coils. However, its ductility and elongation up to 35% according to DIN EN 13601, in combination with its ultimate tensile strength of up to 350 MPa, makes it challenging to machine. Among other additive manufacturing processes, laser powder bed fusion (PBF-LB/M) overcomes existing conventional design restrictions and enables the production of complex components directly from computer aided design models. This is beneficial as it minimizes machining and enables application-specific designs. Utilizing laser radiation at a wavelength of 515 nm, pure copper samples with a density of 99.9%, and electrical conductivity of 100.0% compared to the International Annealed Copper Standard (IACS) are produced.[1] However, most laser powder bed fusion machines today are equipped with single mode fiber laser systems emitting laser radiation in the near-infrared spectrum (NIR). Increasing the wavelength of the laser radiation from 515 to 1064 nm decreases the absorptivity of oxygen-free pure copper powder from 72% to 27%.[1] For this reason, the processing of pure copper using NIR laser radiation is challenging. The addition of carbon nanoparticles,[2] metallic coatings of tin or nickel,[3] and the systematic oxidation of copper powder[4] increase the absorptivity to 67%, 60%, and 58%, respectively, resulting in samples with densities of 98%–99%.[2–4] As impurities such as tin or nickel reduce the electrical conductivity of

copper to approximately 86% IACS or 95% IACS, respectively, at a concentration of 0.09 at. %,[5] the use of pure copper powder is desired. Reducing the particle size distribution (D10–D90) from 17.0–40.1 to 12.1–33.2 μm increases the sample density from 88.4% to 98.1% at a laser power of 175 W, a layer thickness of 20 μm, and a beam diameter of 30 μm.[6] Utilizing a laser power of 400 W, a sample density of 99.8%, and electrical conductivity of 98% IACS is achieved also with a particle size of up to 45 μm at a layer thickness of 30 μm and a beam diameter of 35 μm.[7] At a laser power of 800 W, a sample density of 98.7% is attained for a layer thickness of 50 μm and beam diameter of 78 μm.[8] By applying a multipass scan strategy, the sample density is further increased to 99.1%.[8] Overall, a sample density larger than 98.5% is feasible for increasing beam diameter and layer thickness by raising the laser power used.[6–8] Alternatively, the energy required for melting can be reduced by preheating the substrate plate. At a preheating temperature of 400 °C, a sample density of 99.4% is achieved even with a laser power of 400 W, a beam diameter of 82 μm, and a layer thickness of 30 μm.[9] However, oxidation of the used powder is observed.[9] Considering that the oxygen content of oxidized copper powder remains in the produced sample,[4] process-induced oxidation tends to reduce powder reusability as the oxygen content of material specifications cannot be met. By selecting an appropriate laser power, particle size distribution, beam diameter, and layer thickness, a density of up to 99.8% and electrical conductivity of up to 94% IACS are achieved by using a keyhole welding process.[10] However, fluctuations in the PBF-LB/M process due to the inherent melt pool dynamic, varying thermal conditions, caused by process-induced preheating[11] or varying heat dissipation based on the component geometry, spatters which can absorb portions of the laser radiation, or variations in the powder layer, can cause the keyhole to collapse and form porosity within the resolidified material. For this reason, a heat conduction welding process is advantageous, but due to the intensity peak in the center of the Gaussian laser beam, it is not possible to provide sufficient energy to eliminate lack-of-fusion porosity and concurrently avoid the formation of a keyhole for pure copper.[10]

Changing the intensity distribution of the laser beam from a pure Gaussian distribution to a ring-shaped beam profile consisting of a Gaussian core and a surrounding ring alters the melt pool dynamic.[12–14] Modeling of the temperature field in the PBF-LB/M process based on Péclet numbers shows that by changing the intensity distribution of the laser beam from a Gaussian distribution to a donut-shaped intensity distribution, a specific ring-shaped beam profile without energy in the Gaussian core, the maximum melt pool temperature decreases and evaporation losses are reduced by a factor of more than 2.5 for a CoCr alloy.[15] Furthermore, a reduction of the denudation zone (powder-free zone around the weld track) is reported for a donut-shaped beam profile compared to a Gaussian beam profile for CoCrMo.[16] Numerical simulations of single-tracks for AlSi10Mg also reveal a decrease in vaporization by 40% and mean melt pool velocity by around 20% for a donut-shaped beam profile, resulting in a 35% reduction of spatter.[12] Experimental investigations on process spatter using high-speed imaging show that for Ti6Al4V, a Gaussian beam profile produces 1.4–3.3 times more spatter at a laser power of 300 W, normalized to the weld width, than a ring-shaped beam profile.[17] Observations of the vapor plume angle in PBF-LB/M of AISI 316L exhibit more turbulent fluctuations in the melt pool for a Gaussian beam profile compared to a zero-order Bessel beam, a specific ring-shaped beam profile with a Gaussian core, and several surrounding rings.[13] In addition, a longer solidification time of up to 60% is reported and a smaller thermal gradient is verified by Multiphysics simulation for the Bessel beam.[13] This is consistent with numerical simulations of single-tracks of AlSi10Mg indicating a decrease of the surface tension gradient for a donut-shaped beam profile and, thus, a decrease of the temperature gradient in the melt pool due to the Marangoni effect.[12] Furthermore, a change in the microstructure of Inconel 718 from close to polycrystalline to material with a high texture index is observed by using ring-shaped beam profiles, resulting in a change in the mechanical properties.[18] This is explained by a modification of the temperature gradient and the melt pool geometry.[18] For various materials such as AlSi10Mg,[12] Ti6Al4V,[17] Inconel 718,[18] and AISI 316L,[19] wider but shallower melt pool geometries are reported for ring-shaped beam profiles compared to a Gaussian beam profile. In addition, an enlarged process window is observed for AlSi10Mg (Ref. 12) and AISI 316L.[19] The process window tends to shift toward increasing scan speed and laser power using ring-shaped beam profiles for AISI 316L.[19] Despite increasing laser power, the formation of a keyhole is avoided for Inconel 718 (Ref. 18) and AISI 316L (Ref. 19) due to the reduced peak intensity. Overall, ring-shaped beam profiles tend to reduce the maximum temperature, temperature gradient, and velocity of the melt pool as well as vaporization and spatter, resulting in a more stable welding process.[12–18]

The availability of commercial laser powder bed fusion machines capable of using ring-shaped beam profiles has increased recently. However, the influence of ring-shaped beam profiles on the PBF-LB/M process and the underlying welding process has not yet been investigated for pure copper. In deep-penetration laser beam welding, the use of ring-shaped beam profiles stabilizes the keyhole for Cu-ETP using laser radiation with a wavelength of 515 nm.[20] Therefore, the use of ring-shaped beam profiles offers potential for both heat conduction welding and keyhole welding. In heat conduction welding, a laser power larger than 1000 W can be used to reduce lack-of-fusion porosity without keyhole formation. In keyhole welding, keyhole stabilization enables a PBF-LB/M process which is more robust against fluctuations. For these reasons, the potential of three different ring-shaped beam profiles to produce specimens with a density of more than 99.5% and their respective electrical conductivity is investigated in this study. In order to understand the influence of the ring-shaped beam profiles on the underlying welding process, a single-track experiment is conducted and the metallographic analysis gives insights into the weld geometry. The welding regimes are identified based on the aspect ratio of weld depth to weld width $R = d/w$. A process map based on the classification of single-tracks is created to identify a suitable process window to manufacture cube samples with a laser power of up to 1300 W.

II. EXPERIMENT PROCEDURE AND METHODS

A. Material

Spherical pure copper powder Cu OFHC (ECKART TLS GmbH, Germany) with a purity of larger than 99.95% is used. The particle size distribution, measured by dynamic image analysis using

a Camsizer X2 (Microtrac Retsch GmbH, Germany), is 15.7 μm for D10, 31.8 μm for D50, and 45.5 μm for D90. An oxygen content of 104 ± 2 ppm is measured by inert gas fusion using an Elementrac ONH-p 2 (Eltra GmbH, Germany). A total of five measurements with a weight of 1046 ± 33 mg are carried out and calibrated using three blank samples and three Cu 91000-1003 1 g standards with an oxygen content of 251 ± 3 ppm (Eltra GmbH, Germany). Deoxidized, oxygen-free copper Cu-HCP is used as the substrate material.

B. Experimental setup

Experiments are carried out using a commercial laser powder bed fusion machine DMP Flex 350 (3D Systems Inc., USA) equipped with a programmable fiber laser AFX-1500 (nLIGHT Inc., USA) emitting laser radiation of 1070 nm wavelength. The laser system provides seven switchable ring-shaped beam profiles with defined power ratios (core/ring) between a Gaussian core and a surrounding ring with a maximum output laser power of 1550 W. The laser power behind the optics inside the build chamber is calibrated to the input voltage by means of a calorimetric EC-PowerMonitor (Primes GmbH, Germany) and a maximum laser power of 1359 W is measured.

Laser beam profile measurements are carried out at 200 W using a beam profiling camera SP928, equipped with a beam splitter LBS-300 (Ophir Spiricon Europe GmbH, Germany). Further attenuation of the laser beam behind the beam splitter in front of the CCD sensor is achieved by two neutral density filters totaling ND4. The intensity distributions of the major axis of the investigated ring-shaped beam profiles are shown in Fig. 1. An axisymmetric beam profile consisting of a Gaussian core and two radially shifted Gaussian distributions,

$$I(r) = a_G \exp\left(-\frac{(r-\mu_G)^2}{2\,\sigma_G^2}\right) + a_R \exp\left(-\frac{(r\pm\mu_R)^2}{2\,\sigma_R^2}\right), \quad (1)$$

with the height of the curve peak a, expected value μ, and variance σ^2 of the Gaussian core G, and the surrounding ring R is fitted to the normalized measurement data for the power ratios of 35/65 and 20/80. However, for the power ratio of 10/90, two radially shifted Gaussian distributions,

$$I(r) = a_G \exp\left(-\frac{(r\pm\mu_G)^2}{2\,\sigma_G^2}\right) + a_R \exp\left(-\frac{(r\pm\mu_R)^2}{2\,\sigma_R^2}\right), \quad (2)$$

are selected for the core due to the characteristics of intensity distribution. The calculated beam diameters are provided in Table I. The beam diameter is a decisive factor for the PBF-LB/M process, as it determines the interaction time between the laser beam and a particular point in the powder bed while moving at a constant scan speed.[21] The beam diameter $D4\sigma$ indicates a difference of more than 10% between beam diameters of the ring-shaped beam profiles due to the influence of outward intensity on the calculation. In contrast, considering a certain intensity of, for example, $0.1 \times I_{max}$, there is a difference of less than 2% between the respective beam diameters $D_{0.1}$ of the ring-shaped beam profiles. For this reason, the authors assume a comparable interaction time of the investigated ring-shaped beam profiles.

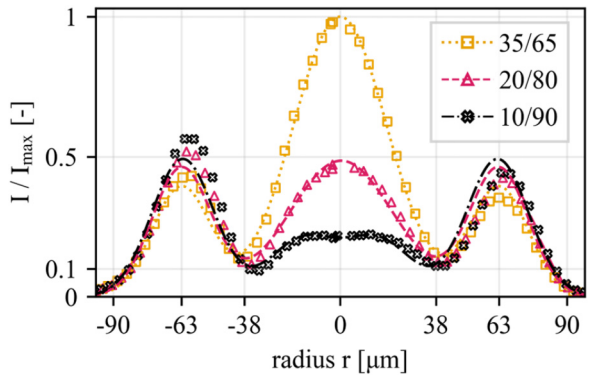

FIG. 1. Intensity distribution for the investigated ring-shaped beam profiles with different power ratios (core/ring) normalized to the maximum intensity I_{max}.

TABLE I. Overview of the calculated beam diameters based on the measured ring-shaped beam profiles.

Parameter			Power ratio 35/65	20/80	10/90
Image					
Beam diameter	$D4\sigma$	(μm)	159.45	171.18	178.12
	$D_{0.1}$	(μm)	164.33	165.93	167.54

C. Design of experiment

1. Single-track experiment

The influence of process parameters and ring-shaped beam profiles on the underlying welding process is studied by welding single-tracks with a length of 10 mm on a substrate plate with an applied powder layer. The limits and step sizes of the full-factorial experimental plan are given in Table II. The experimental plan is run for each ring-shaped beam profile without repetition. To achieve a homogenous powder layer thickness, a pocket is milled into the copper substrate, abrasively blasted, and manually filled with copper powder, whereby a steel blade is used to remove excessive powder. At process conditions, the actual layer thickness is

TABLE II. Overview of the full-factorial experimental plan for the single-track experiment.

Parameter		Limit Lower	Limit Upper	Step size
Laser power P	(W)	700	1300	100
Scan speed v	(mm/s)	200	1000	100

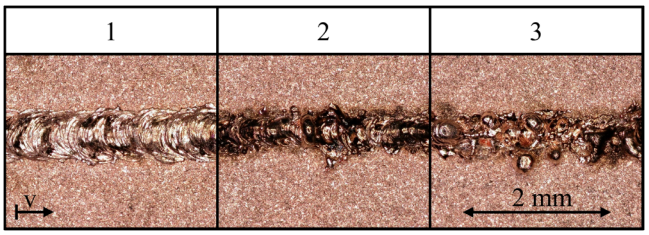

FIG. 2. Top views of single-tracks exemplary for each category: 1. continuous, 2. occasionally broken, and 3. discontinuous.

larger than the nominal layer thickness, for example, four times for AISI 304L.[22] In addition, the process window for continuous weld track formation narrows with increasing layer thickness and tends to shift toward increasing laser power and decreasing scan speed.[23] For these reasons, a powder layer thickness of 90 μm is chosen for the single-track experiment, which corresponds to double the nominal layer thickness of 45 μm of the cube sample experiment.

The single-tracks are categorized along the following three specifications based on the homogeneity of the top view, which is recorded by automatic stitching using a digital microscope VHX-5000 (Keyence Deutschland GmbH, Germany) at 200× magnification. An example for each category is shown in Fig. 2.

(1) Continuous: the single-track topology is homogeneous and continuous without gaps.
(2) Occasionally broken: the single-track topology features irregularities and exhibits a characteristic necking and humping.
(3) Discontinuous: the single-track has separate segments or droplets (balling) with multiple gaps in the weld track.

The onset of irregularities and discontinuities is related to the Plateau–Rayleigh instability caused by the surface tension of the melt pool. The determining factor is the ratio of melt pool length to melt pool width.

Cross sections of the single-tracks are prepared to measure the weld width w and weld depth d as outlined in Fig. 3. The single-tracks are mechanically cut in the center perpendicular to the scan direction and both halves are cold mounted. Grinding and polishing are carried out using silicon carbide grinding paper and diamond suspension followed by OP-S (Struers GmbH, Germany). Specimens are etched in a hot ammonium persulfate solution (10%) to reveal the microstructure. Cross-sectional images are taken using an inverted optical microscope GX-51 equipped with a camera UC30 (Olympus Europa SE & Co. KG, Germany).

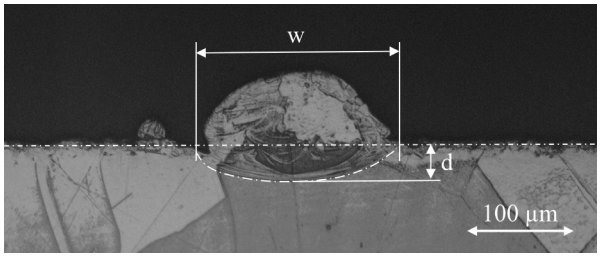

FIG. 3. Exemplary etched single-track cross section with weld width w and weld depth d.

2. Cube sample experiment

The influence of process parameters and ring-shaped beam profiles on the relative density and electrical conductivity are studied by printing cube samples with a size of $10 \times 10 \times 10$ mm^3 on the substrate plate. The limits and step sizes of the full-factorial experimental plan, given in Table III, are selected based on the single-track experiment. The experimental plan is run for each ring-shaped beam profile without repetition. For each run, process parameter combinations are randomly assigned to the cube samples, which are evenly distributed over the entire substrate plate (272×272 mm^2). In addition, the cube samples are rotated by −15° relative to the build direction (z axis) to avoid a parallel alignment of them to the recoater. A layer thickness of 45 μm and a rotation angle of the scan direction between consecutive layers of 67° are defined. A meander hatching strategy is chosen. Preheating the build plate tends to widen the process window and increase the achieved density.[9,21] In addition, process-induced preheating occurs depending on the volume energy density and inter layer time.[11] In order to investigate the potential of the ring-shaped beam profiles, inappropriate process conditions are considered. For this reason, no preheating of the substrate plate and an interlayer time of 180 s are chosen. The oxygen content of the inert argon atmosphere within the build chamber of the PBF-LB/M machine is monitored by oxygen sensors. During all build jobs, the measured values vary between 3.7 and 13.0 ppm.

The cube samples are cut from the substrate plate using wire electrical discharge machining, hot mounted, and ground along their x-z-plane to the center using silicon carbide grinding paper. Final polishing is conducted with diamond suspension. Cross-sectional images (x-z-plane) of the entire cube sample are recorded by automatic stitching using a digital microscope VHX-5000 (Keyence Deutschland GmbH, Germany) at 200× magnification. A white balance is applied. The porosity and density of the cube samples are measured by the ratio of the pore pixel and the total cross-sectional area of the binarized images.

The electrical conductivity of the polished cube samples is measured by the electromagnetic method using an eddy current conductivity meter SigmaCheck 2 with an 8 mm probe PSIG002A and reference standards ASIG010 (Ether NDE Ltd., United Kingdom). A three-point calibration at air, 8.28%, and 100.87%

TABLE III. Overview of the full-factorial experimental plan for the cube sample experiment.

Parameter		Limit		Step size
		Lower	Upper	
Laser power P	(W)	1000	1300	100
Scan speed v	(mm/s)	400	900	100
Hatch distance hd	(μm)	140	180	20

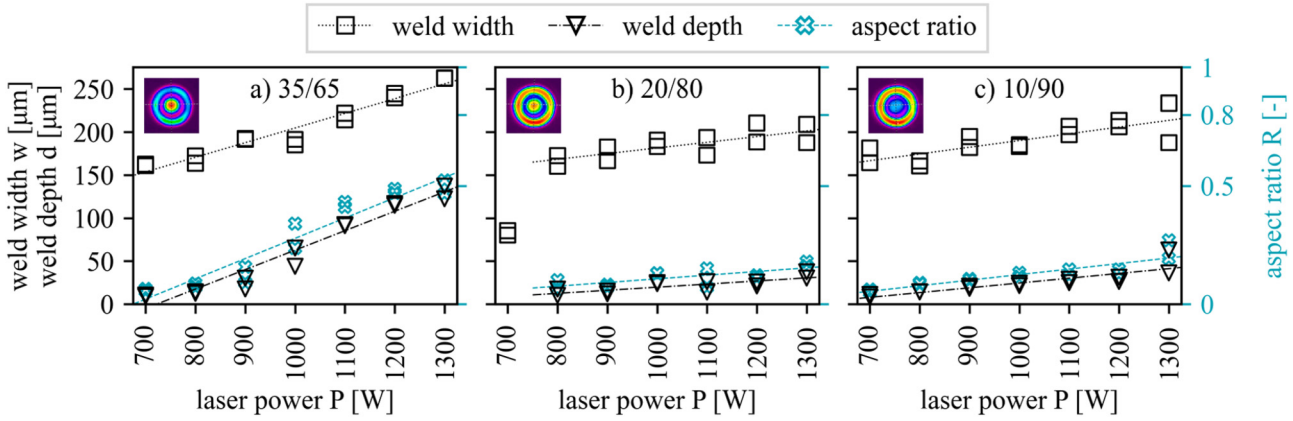

FIG. 4. Diagram of weld width *w*, weld depth *d*, and aspect ratio as a function of laser power *P* at a scan speed of $v = 500$ mm/s for a power ratio of (a) 35/65, (b) 20/80, and (c) 10/90.

IACS is employed. The correctness of the measurement is specified as 0.25% of the measured value. To minimize environmental influence, the temperature of the measurement device, probe, and specimens are stabilized at an ambient temperature of 20 °C in a temperature-controlled room. A total of five measurements are carried out for each cube specimen on different days. The cube samples fulfill the minimum thickness requirement defined by ASTM E1004—17 of 2.6 times the standard depth of penetration δ given by

$$\delta = \frac{660}{\sqrt{f\sigma}} = 0.269\,\text{mm}, \tag{3}$$

with examination frequency $f = 60$ kHz and electrical conductivity $\sigma = 101\%$ IACS of oxygen-free copper.

III. RESULTS AND DISCUSSION

In the following, the experimental results of the single-track and cube sample experiments are presented and the influence of the process parameters and ring-shaped beam profiles are discussed.

The median difference between both evaluated sides of the single-track experiment is approximate 15 μm for weld width and approximate 6.4 μm for weld depth. The standard deviation of the electrical conductivity of the cube experiment has a median value of 0.23% IACS.

A. Influence of laser power on single-track geometry

An increase in weld width *w*, weld depth *d*, and aspect ratio *R* with increasing laser power *P* for all investigated ring-shaped beam profiles can be observed in Fig. 4 for a typical data set at a scan speed of $v = 500$ mm/s. A linear fit is used to reveal the respective trend. No weld depth is detectable for a laser power of 700 W at a power ratio of 20/80. In addition, the corresponding weld width exhibits a deviation from the rest of the data series and was, therefore, excluded from the trend line.

At a laser power of 1300 W, the widest and deepest weld geometry is found for a power ratio of 35/65 and a difference to the weld depth and weld width of 20/80 and 10/90 can be recognized. The corresponding cross sections, displayed in Fig. 5, also reveal a deeper and wider melt pool for a power ratio of 35/65 compared to the shallower and narrower melt pools of 20/80 and 10/90. This can be explained by peak intensity and intensity distribution. For a power ratio of 35/65, the intensity peak in the center, shown in Fig. 1, causes a temperature gradient in the melt pool from the center outward and, therefore, an outward flow due to the Marangoni effect. In addition, vaporization and inherent recoil pressure induce shear stresses on the molten surface. As a result, the melt in the center is pulled outward and a depression is formed. The melt from the center with a higher temperature than in the outer area assists in outward heat dissipation heading to an extension of the melt pool width.[14] As the laser power increases, vaporization and melt pool velocity rise, which tend to a deeper depression.[12] The aspect ratio approaches $R = 0.5$, which

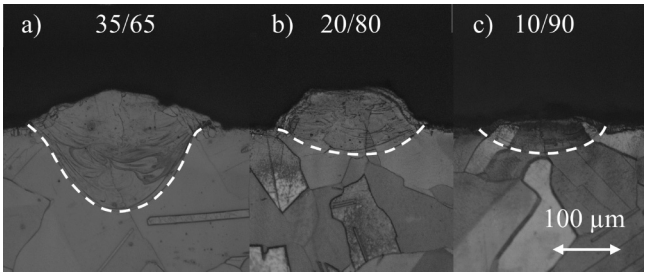

FIG. 5. Etched single-track cross sections at a laser power of $P = 1300$ W and a scan speed of $v = 500$ mm/s for a power ratio of (a) 35/65, (b) 20/80, and (c) 10/90.

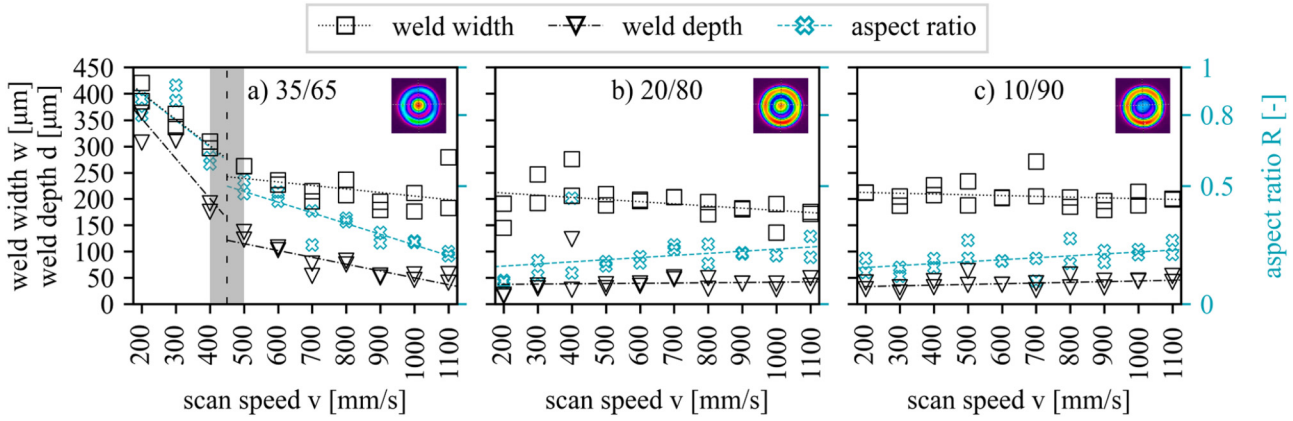

FIG. 6. Diagram of weld width *w*, weld depth *d*, and aspect ratio *R* as a function of scan speed *v* at a laser power of *P* = 1300 W for a power ratio of (a) 35/65, (b) 20/80, and (c) 10/90.

corresponds approximately to an inclination angle of the melt front of 45°.[24] At this point, multireflection can occur, increasing the absorptivity from 20 to up to 53% for a fully developed keyhole ($R > 0.8$) and, thus, tend to enlarge the weld width and weld depth.[21,25] Increasing the power ratio of the surrounding ring for 20/80 and 10/90 reduces the peak intensity in comparison to 35/65, and, thus, the maximum temperature as well as melt flow velocity and vaporization tends to decrease.[12,26] Consequently, the depression is shallower and narrower compared to the power ratio of 35/65. The absorption coefficient of copper in the heat conduction welding regime of only 20% in combination with thermal conductivity inhibits the expansion of the melt pool resulting in the shallow and narrow weld geometry for a power ratio of 20/80 and 10/90 compared to 35/65.[21,25] This is confirmed by comparing the mean weld width to the beam diameter $D_{0.1}$, given in Table I. For the power ratios of 20/80 and 10/90, a mean weld width of approximately 198 and 210 μm at the beam diameter $D_{0.1}$ of around 166 and 168 μm is measured, respectively, while a mean weld width of approximately 262 μm at the beam diameter $D_{0.1}$ of around 164 μm is measured for 35/65.

At a laser power of 800 W, all investigated ring-shaped beam profiles have comparable weld widths and weld depths. This indicates that the intensity of the power ratio 35/65 is not sufficient to cause a deeper depression than for 20/80 and 10/90.

Considering the aspect ratio and the corresponding trend line for power ratios of 20/80 and 10/90, assuming that the trend remains the same, a laser power of approximate 2600 W is required for the onset of keyhole formation. Therefore, a heat conduction welding process for pure copper in PBF-LB/M at laser powers larger than 1300 W is conceivable. However, ring-shaped beam profiles demonstrate keyhole stabilization and thus, the use of laser powers larger than 1300 W is also conceivable for a power ratio of 35/65.[20]

B. Influence of scan speed on single track geometry

In Fig. 6, weld width *w*, weld depth *d*, and aspect ratio *R* of the single-tracks at a laser power *P* of 1300 W are plotted over the scan speed *v* for all investigated ring-shaped beam profiles. A transition area from conduction welding ($R < 0.5$) to keyhole formation ($R \geq 0.5$) and keyhole welding ($R > 0.8$) is marked in gray. A linear fit is used to reveal the trend in the respective intervals below and above the transition area. Keyhole formation is only present for a power ratio of 35/65 for scan speeds below 500 mm/s and is accompanied by a jump in weld width, weld depth, and aspect ratio due to the onset of multireflection, and thus, an increase in absorptivity from 20 up to 53%.[25]

Considering the aspect ratio, there is again a difference between the power ratio of 35/65 compared to 20/80 and 10/90. Whereas the aspect ratio decreases for the power ratio of 35/65 with increasing scan speed, it increases for 20/80 and 10/90. For a power ratio of 35/65, the decrease in the aspect ratio results from the simultaneous decline in weld width and weld depth due to the reduction in energy input given by the laser power *P* multiplied by the interaction time $t_i = D_{0.1}/v$. For a power ratio of 20/80 and 10/90, there is also a decline in weld width with increasing scan speed, but the weld depth increases slightly up to 26 μm, which leads to an increase in the aspect ratio. This indicates that the decrease in energy input has no impact on the weld depth for a power ratio of 20/80 and 10/90. The authors assume that the increase in scan speed leads to an increase in melt pool velocity, and, thus, the melt in the center tends to be pulled outward more strongly, which creates a deeper depression.[12]

In Fig. 7, the weld depth *d* over the scan speed *v* for a power ratio of 35/65 at laser powers *P* of 900, 1000, and 1100 W is shown. A transition area from conduction welding to keyhole formation and keyhole welding is marked in gray for 1100 W. A linear trend is used for 900 and 1100 W, but no steady trend is evident for 1000 W. As the scan speed increases, the weld depth decreases for a laser power of 1100 W, similar to a laser power *P* of 1300 W in Fig. 6. However, an increase in weld depth with increasing scan speed is present at a laser power of 900 W, which is similar to the power ratios of 20/80 and 10/90 at a laser power *P* of 1300 W in Fig. 6. At a laser power of 1000 W, a fluctuating behavior can be

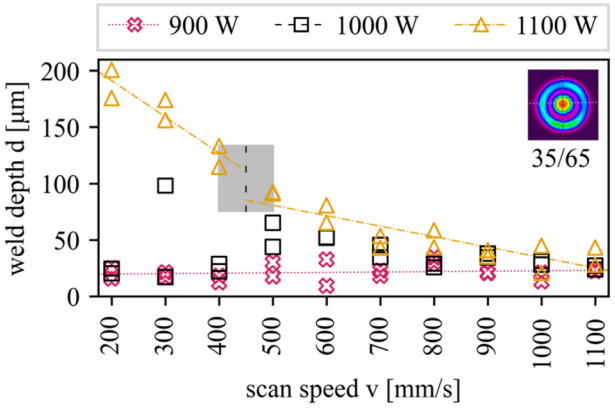

FIG. 7. Diagram of weld depth d as a function of scan speed v for a power ratio of 35/65 at a laser power of 900, 1000, and 1100 W.

observed. This indicates a threshold power at which the welding behavior alters and the depth of the depression increases. Welding experiments conducted on Cu-ETP using laser radiation of 515 nm wavelength also show such a threshold for a ring-shaped beam profile with a power ratio of 0/100 between a laser power of 2000 and 3000 W.[20] For this reason, a threshold is also expected for power ratios of 20/80 and 10/90 at laser powers larger than 1300 W.

C. Process map of single-track experiment

Figure 8 shows process maps of the single-tracks for the investigated ring-shaped beam profiles with regard to the process parameters' laser power P and scan speed v. The color and filling of the marker indicate the categorization of the weld track according to the definition. In addition, characteristics such as keyhole welding, given by a mean aspect ratio $\bar{R} \geq 0.8$, poor penetration, which is defined by a mean weld depth below one-third of the nominal layer thickness of the cube experiment $\bar{d} \leq 15\,\mu$m, or balling are highlighted by the corresponding marker.[21] The dashed outlined area indicates the parameter range selected for the density cube experiment.

At a laser power of 700 and 800 W, poor penetration can be observed for all investigated ring-shaped beam profiles. For power ratios of 20/80 and 10/90, lower intensities and higher ring power ratios compared to 35/65 also lead to poor penetration at a laser power of 900 W. In addition, poor bonding can be observed even at a laser power of 1000 W for a power ratio of 10/90 because only one of the two cross sections has a weld depth of 5.9 μm. In contrast, the intensity peak in the Gaussian center for the power ratio 35/65 leads to a keyhole welding process at a laser power of 1300 W and a scan speed of 200 and 300 mm/s.

For all ring-shaped beam profiles, no influence on the homogeneity of the single-tracks is recognizable for the laser power, but for the scan speed. At a laser power of at least 1000 W, continuous weld tracks form up to a scan speed of 600, 800, and 700 mm/s for power ratios of 35/65, 20/80, and 10/90, respectively. This can be explained by the Plateau–Rayleigh instability due to the surface tension of the melt pool. For a segmental cylinder, instability occurs when the length-to-width ratio of the melt pool exceeds $1.22 \times \pi$.[27] Considering Fig. 6 at a laser power of 1300 W, the power ratio of 35/65 has a deeper melt pool compared to 20/80 and 10/90 for all investigated scan speeds. As the laser power and interaction time are similar, the absorptivity of the power ratio 35/65 is higher than for 20/80 and 10/90 and, therefore, a longer melt pool is expected. The weld width of all investigated ring-shaped beam profiles is comparable above a scan speed of 500 mm/s. As a result of the larger length-to-width ratio, instability occurs for the power

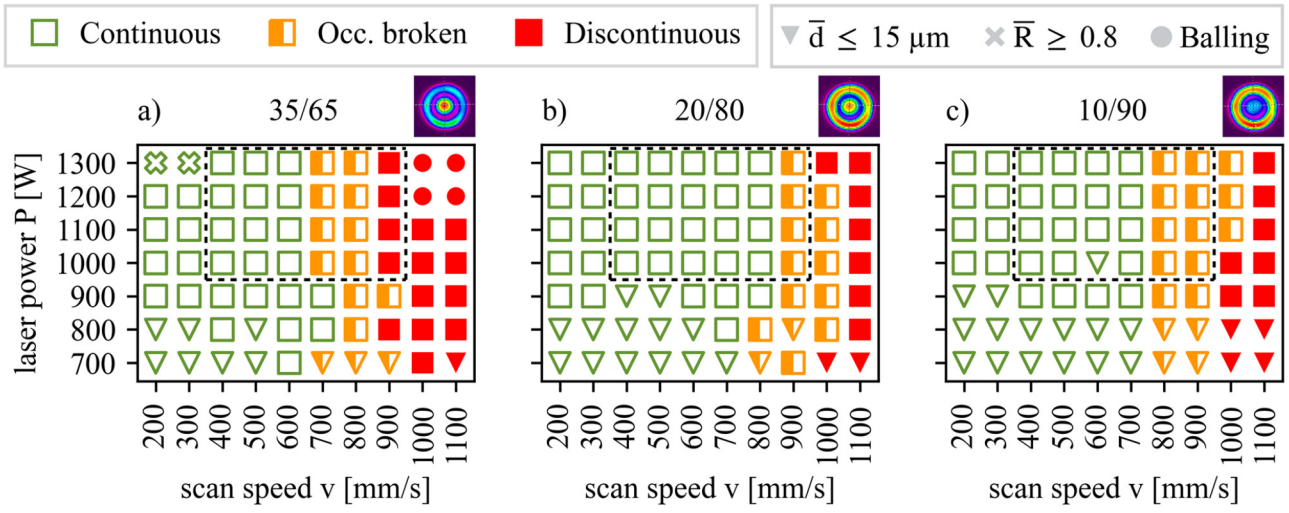

FIG. 8. Process maps of the single-track experiments with regard to laser power P and scan speed v for a power ratio of (a) 35/65, (b) 20/80, and (c) 10/90.

ratio of 35/65 above a scan speed of 600 mm/s. In addition, the higher temperature, melt pool velocities, and vaporization of the power ratio of 35/65 compared to 20/80 and 10/90 lead to intensified turbulence in the melt pool, which tends to have a negative impact on stability. The power ratio 20/80 has a more uniform melt pool temperature compared to 10/90,[26] so instabilities occur at scan speeds above 800 mm/s, while 10/90 already exhibits instabilities at 700 mm/s. Necking and humping, which are preliminary to full instability, are the main characteristics of the occasionally broken single-tracks. Elongated separate segments are formed for all discontinuous single-tracks. Balling, which depends on lack-of-fusion and wetting behavior, occurs only for the power ratio of 35/65 at a laser power of at least 1200 W and a scan speed of at least 1000 mm/s.[28] The absence of balling indicates better wettability for the power ratios of 20/80 and 10/90 compared to 35/65, as the respective weld depths shown in Fig. 6 are comparable.

The process window for the cube sample experiment is chosen to avoid keyhole welding and poor penetration, but still cover and even exceed the process window of 20/80.

D. Influence of the process parameters on the density and electrical conductivity of cube samples

Figure 9 shows the influence of the ring-shaped beam profile as well as process parameters laser power P, scan speed v, and hatch distance hd on the mean density $\overline{\rho_{ROI}}$, indicated with a filled marker, and mean electrical conductivity $\bar{\sigma}$, indicated with an unfilled marker, of all cube samples. Comparable trends for mean density and mean electrical conductivity can be observed for all process parameters. Compared to 20/80 and 10/90, higher density values and electrical conductivity are achieved for the power ratio of 35/65 at identical laser powers, hatch distances, and scan speeds. The power ratios of 20/80 and 10/90 are at a comparable level, whereby 20/80 attain a lower density but higher electrical conductivity than 10/90. This can be explained by the weld geometry. Figure 4 shows that the weld geometry for the power ratio of 35/65 is wider and deeper than for 20/80 and 10/90, which are at a comparable level. With an increasing weld width and weld depth, the overlap of adjacent weld tracks improves at identical hatch distances and remelting of the underlaying layer enhances, which tends to reduce lack-of-fusion defects. This is confirmed by the cross sections shown in Fig. 10. Representative sections of $2 \times 2\ \mathrm{mm}^2$ in size are taken from the center to improve the visibility of the pores. Compared to the power ratios of 20/80 and 10/90, the power ratio of 35/65 exhibits a lower quantity and smaller size of irregular shaped pores across all presented cross sections.

With increasing laser power, the density and electrical conductivity increase due to a deeper and wider weld geometry, as shown in Fig. 4. Comparing the cross sections displayed in Figs. 10(a) and 10(b), it is evident that the quantity and size of irregular shaped pores decrease with increasing laser power for all investigated ring-shaped beam profiles. For the power ratio of 35/65, the electrical conductivity increases steeply compared to 20/80 and 10/90. This may be due to keyhole formation ($R \geq 0.5$) at a laser power of 1200 and 1300 W as well as a scan speed of up to 400 mm/s, resulting in a jump in weld depth and weld width, as shown in Fig. 6, and, thus, improves overlap and remelting. In PBF-LB, an increase in density is reported with increasing laser power until no lack-of-fusion pores within the resolidified material are present. However, a transition point exists at which the density decreases, as the amount of gas pores or keyhole pores in the resolidified material increases.[10,12,28] This trend is not evident in Fig. 9 for any of the investigated ring-shaped beam profiles. Furthermore, the cross section for the power ratio of 35/65 at a laser power of 1300 W and a scan speed of 400 mm/s shown in Fig. 10(a) exhibits irregular shaped pores rather than near-spherically shaped pores, indicating lack-of-fusion pores rather than gas or keyhole pores.[28] For these reasons, a further increase in laser power is conceivable.

As the hatch distance increases, the overlap of adjacent weld tracks reduces, and, thus, the part density tends to decrease. This is

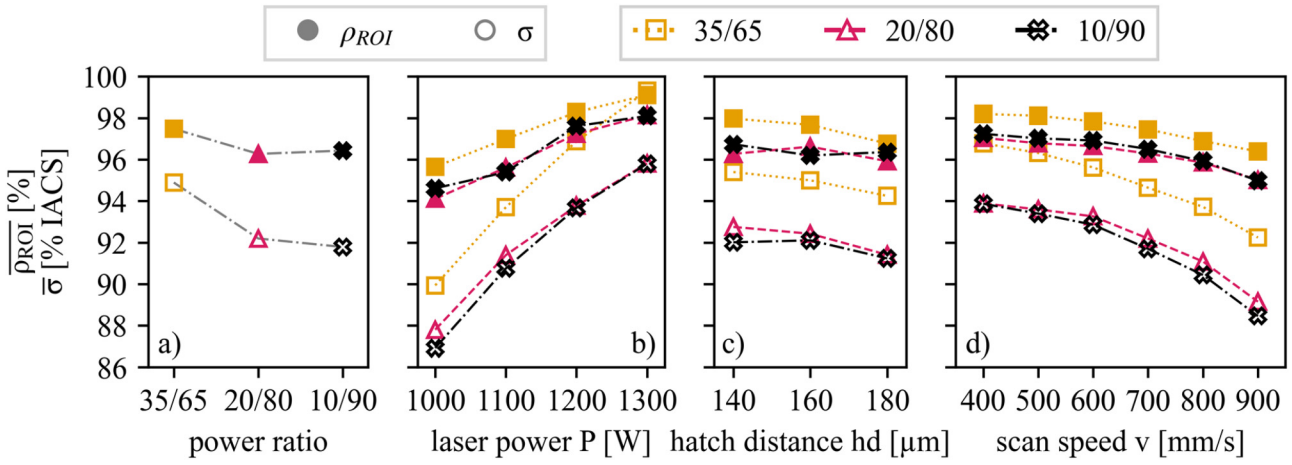

FIG. 9. Diagram of mean density $\overline{\rho_{ROI}}$ and mean electrical conductivity $\bar{\sigma}$ of all cube samples as a function of the process parameters: (a) power ratio, (b) laser power P, (c) hatch distance hd, and (d) scan speed v.

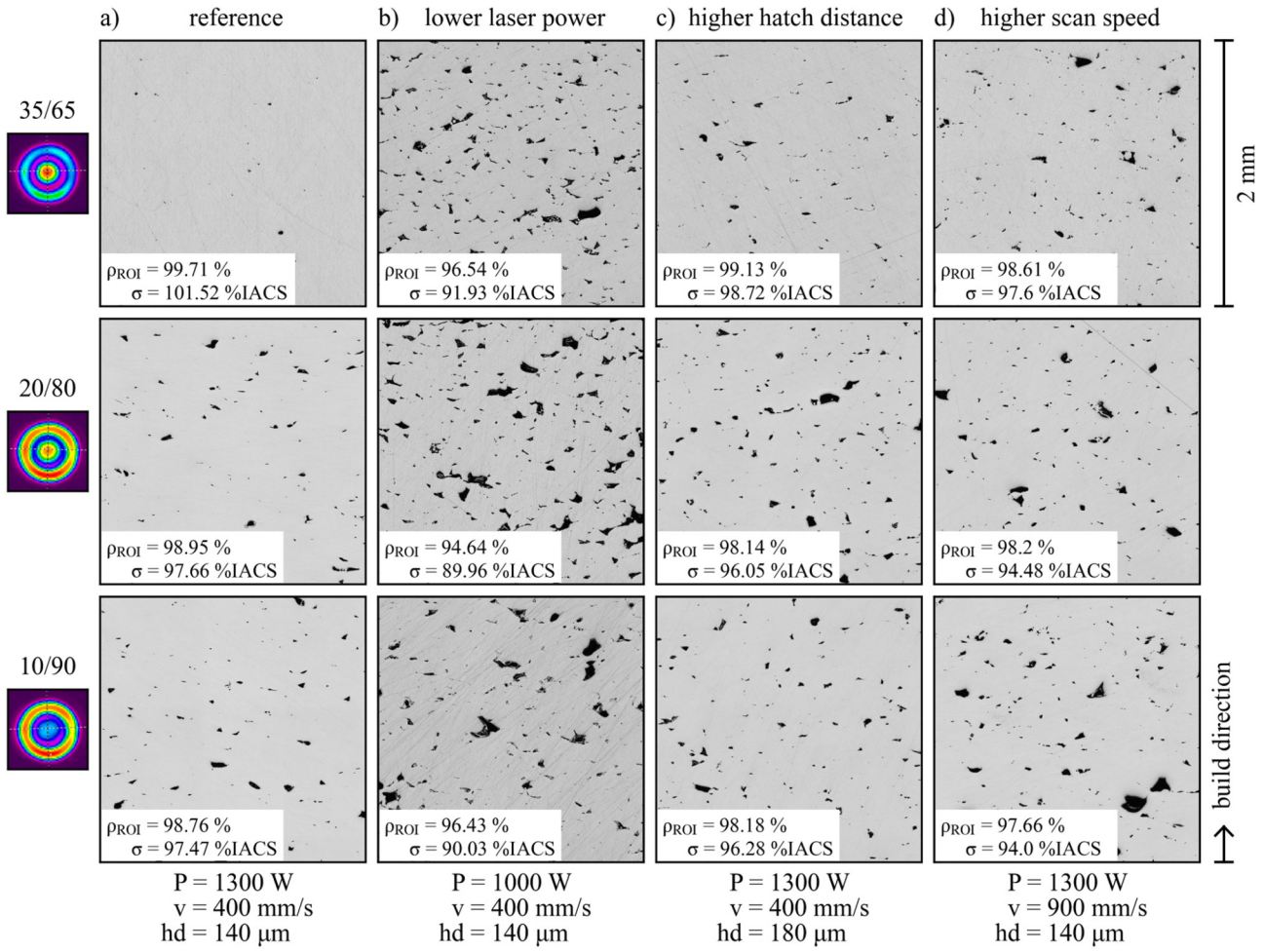

FIG. 10. Overview of cross sections of the cube samples and their respective density and electrical conductivity manufactured with (a) reference process parameters, (b) lower laser power, (c) higher hatch distance, and (d) higher scan speed for all investigated ring-shaped beam profiles.

confirmed by an increase in the quantity of lack-of-fusion pores between the cross sections shown in Figs. 10(a) and 10(c) for all ring-shaped beam profiles. For the power ratio of 35/65, an increase in the size of the lack-of-fusion pores is evident with increasing hatch distance. The declining trend is apparent in Fig. 9 for the density of the power ratio 35/65 and the electrical conductivity of all ring-shaped beam profiles. However, the density of the power ratios of 20/80 and 10/90 differ from this trend. Comparing the density with the corresponding electrical conductivity, the authors assume that the reason for this is related to density measurement.

An increasing decline in density and electrical conductivity is observed with increasing scan speed for all ring-shaped beam profiles in Fig. 9. This can be explained by melt pool instabilities and weld geometry. Considering the process map shown in Fig. 8, instabilities occur at scan speeds of 600–800 mm/s, which tend to cause lack-of-fusion pores. As a result of the 100 mm/s larger process window, the power ratio of 20/80 exhibits a higher electrical conductivity than 10/90 at scan speeds of at least 500 mm/s, whereby the density is at a comparable level. In contrast, the power ratio of 35/65 has the narrowest process window with scan speeds of up to 600 mm/s and should, therefore, exhibit the steepest decline. However, this is not evident in Fig. 9, indicating that the deeper and wider melt pool of the power ratio 35/65 compared to 20/80 and 10/90 shown in Fig. 6 counteracts the influence of instability by enhanced remelting and overlap. However, the weld width and weld depth decrease for a power ratio of 35/65 with increasing scan speed, which decreases the overlap and remelting and, thus, reduces the density and electrical conductivity. For power ratios of 20/80 and 10/90, a decrease in weld width is observed, while the weld depth increases. A less steep decline is, therefore, expected but is not evident in Fig. 9. Comparing the cross sections in Figs. 10(a) and 10(d), an increase in the quantity and size of lack-of-fusion

TABLE IV. Overview of the cube samples with the highest electrical conductivity and the respective density for each ring-shaped beam profile.

Parameter		Power ratio 35/65	20/80	10/90
Laser power P	(W)	1300	1300	1300
Scan speed v	(mm/s)	400	400	400
Hatch distance hd	(μm)	160	140	140
Density ρ_{ROI}	(%)	99.77	98.95	98.76
Electrical conductivity σ	(%IACS)	101.62	97.66	97.47

pores is evident for all ring-shaped beam profiles. A categorization of the pores based on their cause of formation is not possible from the cross sections.

Noticeable is the parallel course of density and electrical conductivity in Fig. 9. The linear regression of electrical conductivity over the density of all cube samples gives

$$\sigma(\rho_{ROI}) = 2.118 \times \rho_{ROI} - 111.916, \quad (4)$$

with a coefficient of determination $R^2 = 0.89$ and a root mean square error of RMSE = 1.33% IACS. Table IV summarizes the cube samples with the highest electrical conductivity for each ring-shaped beam profile as well as the respective process parameters and density values. The aspect ratios of the respective single-tracks reveal keyhole formation, with a mean aspect ratio of 0.61, for a power ratio of 35/65. Whereas heat conduction welding is observed for a power ratio of 20/80 and 10/90, exhibiting a mean aspect ratio of 0.29 and 0.17, respectively.

IV. CONCLUSION

Ring-shaped beam profiles demonstrate advantages in stabilizing the PBF-LB/M process and improve productivity, but pure copper has not yet been processed. Therefore, the potential of three ring-shaped beam profiles with different power ratios between a Gaussian core and a surrounding ring (core/ring) to produce specimens with a density of more than 99.5% and their respective electrical conductivity is investigated. In order to understand the welding process, a single-track experiment is conducted and metallographic analysis gives insights into the weld geometry.

For all ring-shaped beam profiles, an increase in laser power leads to an increase in weld width and weld depth. A decrease in weld width is observed as the scan speed increases. However, the influence of the scan speed on the weld depth depends on the used ring-shaped beam profile and laser power. For a power ratio of 35/65, a laser power of 1100 W is sufficient to form a deeper and wider weld geometry compared to 20/80 and 10/90, which have a shallow and narrow weld geometry even at a laser power of 1300 W.

A linear relationship is observed between the density and electrical conductivity of the cube samples. The highest electrical conductivity of 101.62% IACS is achieved with a power ratio of 35/65 and a density of 99.77% is measured. The power ratios of 20/80 and 10/90 show comparable results with densities of 98.95% and 98.76%, and electrical conductivities of 97.66% and 97.47% IACS, respectively. The aspect ratios of the respective single-tracks reveal keyhole formation for a power ratio of 35/65, whereas heat conduction welding is observed for a power ratio of 20/80 and 10/90.

Our findings indicate that a further increase in laser power tends to enhance the density and electrical conductivity for all ring-shaped beam profiles. A further increase in the weld depth and weld width is expected, which facilitates higher hatch distances. The scan speed may be raised until the material requirements with regard to density and electrical conductivity are no longer met. This has the potential to improve the productivity of the PBF-LB/M process. Consequently, further research into ring-shaped beam profiles in PBF-LB/M of pure copper using laser powers of more than 1300 W is necessary. In particular, investigations into the stability of the welding process, either by stabilizing the keyhole or using a heat conduction welding process, are required.

ACKNOWLEDGMENTS

The work described is financed with funds from the state innovation funding of the Free and Hanseatic City of Hamburg under Reference No. LIF-004. The authors would like to thank Christian Schröter from Optoprim Germany GmbH for providing the laser system. The provision is gratefully acknowledged.

AUTHOR DECLARATIONS

Conflict of Interest

Optoprim Germany GmbH provided the laser system for a three-month period, but had no influence on the experiments, analysis, and publication of the results.

Author Contributions

Alexander Bauch: Conceptualization (lead); Data curation (lead); Formal analysis (lead); Funding acquisition (lead); Investigation (lead); Methodology (lead); Project administration (lead); Resources (equal); Supervision (lead); Visualization (lead); Writing – original draft (lead). **Philipp Kohlwes:** Conceptualization (supporting); Resources (equal); Writing – review & editing (equal). **Ingomar Kelbassa:** Writing – review & editing (equal).

REFERENCES

[1]S. Gruber, L. Stepien, E. López, F. Brueckner, and C. Leyens, "Physical and geometrical properties of additively manufactured pure copper samples using a green laser source," Materials **14**, 3642 (2021).
[2]S. D. Jadhav, S. Dadbakhsh, J. Vleugels, J. Hofkens, P. Van Puyvelde, S. Yang, J.-P. Kruth, J. Van Humbeeck, and K. Vanmeensel, "Influence of carbon nanoparticle addition (and impurities) on selective laser melting of pure copper," Materials **12**, 2469 (2019).
[3]V. Lindström, O. Liashenko, K. Zweiacker, S. Derevianko, V. Morozovych, Y. Lyashenko, and C. Leinenbach, "Laser powder bed fusion of metal coated copper powders," Materials **13**(16), 3493 (2020).
[4]S. D. Jadhav, J. Vleugels, J.-P. Kruth, J. Van Humbeeck, and K. Vanmeensel, "Mechanical and electrical properties of selective laser-melted parts produced from surface-oxidized copper powder," Mater. Des. Process. Commun. **2**, e94 (2020).
[5]F. Pawlek and K. Reichel, "Der Einfluß von Beimengungen auf die elektrische Leitfähigkeit von Kupfer," Int. J. Mater. Res. **47**, 347–356 (1956).

[6]M. Sinico, G. Cogo, M. Benettoni, I. Calliari, and A. Pepato, "Influence of powder particle size distribution on the printability of pure copper for selective laser melting" (2019).
[7]T. Stoll, P. Trautnitz, S. Schmiedeke, J. E. Franke, and N. Travitzky, in *Process Development for Laser Powder bed Fusion of Pure Copper, Laser 3D Manufacturing VII, San Francisco, CA, 4-6 February 2020* (SPIE, Bellingham, WA, 2020), p. 46.
[8]M. Colopi, A. G. Demir, L. Caprio, and B. Previtali, "Limits and solutions in processing pure Cu via selective laser melting using a high-power single-mode fiber laser," Int. J. Adv. Manuf. Technol. **104**, 2473–2486 (2019).
[9]M. Malý, D. Koutný, L. Pantělejev, L. Pambaguian, and D. Paloušek, "Effect of high-temperature preheating on pure copper thick-walled samples processed by laser powder bed fusion," J. Manuf. Processes **73**, 924–938 (2022).
[10]S. D. Jadhav, L. R. Goossens, Y. Kinds, B. Van Hooreweder, and K. Vanmeensel, "Laser-based powder bed fusion additive manufacturing of pure copper," Addit. Manuf. **42**, 101990 (2021).
[11]G. Mohr, K. Sommer, T. Knobloch, S. J. Altenburg, S. Recknagel, D. Bettge, and K. Hilgenberg, "Process induced preheating in laser powder bed fusion monitored by thermography and its influence on the microstructure of 316L stainless steel parts," Metals **11**, 1063 (2021).
[12]T. M. Wischeropp, "Advancement of selective laser melting by laser beam shaping," Ph.D. dissertation, Hamburg University of Technology, 2022.
[13]T. U. Tumkur, T. Voisin, R. Shi, P. J. Depond, T. T. Roehling, S. Wu, M. F. Crumb, J. D. Roehling, G. Guss, S. A. Khairallah, and M. J. Matthews, "Nondiffractive beam shaping for enhanced optothermal control in metal additive manufacturing," Sci. Adv. **7**, eabg9358 (2021).
[14]L. Han and F. W. Liou, "Numerical investigation of the influence of laser beam mode on melt pool," Int. J. Heat Mass Transfer **47**, 4385–4402 (2004).
[15]S. N. Grigoriev, A. V. Gusarov, A. S. Metel, T. V. Tarasova, M. A. Volosova, A. A. Okunkova, and A. S. Gusev, "Beam shaping in laser powder bed fusion: Péclet number and dynamic simulation," Metals **12**, 722 (2022).
[16]A. S. Metel, M. M. Stebulyanin, S. V. Fedorov, and A. A. Okunkova, "Power density distribution for laser additive manufacturing (SLM): Potential, fundamentals and advanced applications," Technologies **7**, 5 (2019).
[17]P. Kohlwes, "Prozessstabile additive fertigung durch spritzerreduziertes laserstrahlschmelzen," Ph.D. dissertation, Hamburg University of Technology, 2024.
[18]J. D. Pérez-Ruiz, F. Galbusera, L. Caprio, B. Previtali, L. N. L. de Lacalle, A. Lamikiz, and A. G. Demir, "Laser beam shaping facilitates tailoring the mechanical properties of IN718 during powder bed fusion," J. Mater. Process. Technol. **328**, 118393 (2024).
[19]J. Grünewald, F. Gehringer, M. Schmöller, and K. Wudy, "Influence of ring-shaped beam profiles on process stability and productivity in laser-based powder bed fusion of AISI 316L," Metals **11**, 1989 (2021).
[20]F. Kaufmann, A. Maier, J. Schrauder, S. Roth, and M. Schmidt, "Influence of superimposed intensity distributions on weld seam quality and spatter behavior during laser beam welding of copper with green laser radiation," J. Laser Appl. **34**, 042008 (2022).
[21]A. Bauch and D. Herzog, "Influence of temperature and beam size on weld track shape in laser powder bed fusion of pure copper using near-infrared laser system," J. Laser Appl. **36**, 012007 (2024).
[22]T. Liu, C. S. Lough, H. Sehhat, Y. M. Ren, P. D. Christofides, E. C. Kinzel, and M. C. Leu, "In-situ infrared thermographic inspection for local powder layer thickness measurement in laser powder bed fusion," Addit. Manuf. **55**, 102873 (2022).
[23]I. Yadroitsev and I. Smurov, "Selective laser melting technology: From the single laser melted track stability to 3D parts of complex shape," Phys. Procedia **5**, 551–560 (2010).
[24]R. Fabbro, M. Dal, P. Peyre, F. Coste, M. Schneider, and V. Gunenthiram, "Analysis and possible estimation of keyhole depths evolution, using laser operating parameters and material properties," J. Laser Appl. **30**, 032410 (2018).
[25]L. Gargalis, J. Ye, M. Strantza, A. Rubenchik, J. W. Murray, A. T. Clare, I. A. Ashcroft, R. Hague, and M. J. Matthews, "Determining processing behaviour of pure Cu in laser powder bed fusion using direct micro-calorimetry," J. Mater. Process. Technol. **294**, 117130 (2021).
[26]V. Holla, P. Kopp, J. Grünewald, K. Wudy, and S. Kollmannsberger, "Laser beam shape optimization in powder bed fusion of metals," Addit. Manuf. **72**, 103609 (2023).
[27]I. Yadroitsev, A. Gusarov, I. Yadroitsava, and I. Smurov, "Single track formation in selective laser melting of metal powders," J. Mater. Process. Technol. **210**, 1624–1631 (2010).
[28]C. Tang, J. L. Tan, and C. H. Wong, "A numerical investigation on the physical mechanisms of single track defects in selective laser melting," Int. J. Heat Mass Transfer **126**, 957–968 (2018).